

2012-8-24

Tomography of Diffraction-Based Focusing Operators

Luiz Alberto Santos, *et al.*

© 2012 Society of Exploration Geophysicists.

Tomography of diffraction-based focusing operators

Luiz Alberto Santos¹, Webe Joao Mansur², and George A. McMechan³

ABSTRACT

Diffractions carry the same kinematic information provided by common focus point operators (CFPOs). Thus CFPO and diffraction time trajectories may be used separately, or combined into a single unified tomography for velocity analysis. Velocity estimation by tomography of CFPOs reduces the depth-velocity ambiguity compared to two-way time tomography. CFPO estimation is complicated where there are event discontinuities and diffractions. This problem is overcome by using the kinematic information in diffractions in near-offset common-offset gathers. The procedure is illustrated using synthetic data, and a single-channel field seismic profile from the Blake Ridge (off the east coast of the United States). The results show the effectiveness of the proposed method for estimation of velocity from single channel seismic data, and for refinement of the velocity field from multichannel data. Both applications are cost-competitive.

INTRODUCTION

An interval velocity field for depth imaging may be obtained by migration velocity analysis (MVA) or by ray-tracing-based (RT-based) tomography. In MVA, the image of a point, sampled several times by different shots, will be flattened at the same depth in all panels (common-shot, common-receiver, common-offset gathers) after depth migration with the correct velocity. Al-Yahya (1989) iterates to flatten events in common-receiver gathers; McKay and Abma (1992) compare focusing and migrated depths in common-shot gathers. Harlan et al. (1984) isolate diffraction events from coherent reflections and quantify focusing using statistical tools. Sava et al. (2005) focus diffractions to estimate interval velocities. Fomel et al. (2007) separate diffractions from reflections in

poststack data and focus diffractions by velocity continuation (Fomel, 2003). Reshef and Landa (2009) use postmigrated dip angles in common-image gathers to distinguish diffractions from reflections and to estimate velocity. Dell and Gajewski (2011) use common-reflection-surface attributes to separate diffractions and to perform poststack time migration velocity analysis. Burnett et al. (2011) combine velocity continuation methods with path-integrals for diffraction imaging.

Billette et al. (1998) and Woodward et al. (2008) summarize the evolution of the RT-based tomographic methods. Most of them invert to two-way reflection time data. The common focus point (CFP) technique is the only one that uses one-way time data to reduce the velocity-depth ambiguity (Cox, 2004). Use of CFPs splits the conventional reflection tomography of Bishop et al. (1985) at the reflection point to work in a one-way transmission tomography context, and thus has advantages over MVA-based and two-way RT-based techniques.

All implementations of CFP-based tomography (Hegge et al., 1996, 1997, 1998, 1999; Kabir, 1997; Hegge, 2000; Kabir and Verschurr, 2000; Cox, 2004; Liu et al., 2006) require CFP operators (CFPOs). Conventional methods to estimate CFPOs use multioffset data (Berkhout, 1997a, 1997b; Thorbecke, 1997; Bolte, 2003; Rijzen et al., 2004) and they work better if the reflections are laterally continuous. In highly deformed regions, reflector continuity is broken by faults that generate edge diffractions. Tight folds with small radii of curvature behave like edges and generate responses similar to diffractions, which are undesired noise for conventional CFPO estimation, but, as shown below, they are very useful for CFP velocity estimation. Real diffractions from points carry the same kinematic responses as CFPOs.

It is necessary to define events that behave as real diffractions, to combine with conventional CFPOs, or to use alone, in tomographic inversion. Through modeling and practical observations, we distinguish between real and apparent diffractions (Appendix A).

Applications are illustrated, with a synthetic data set for a thrust-detachment model, and with field data. The synthetic model contains highly deformed and non-deformed regions. Two synthetic

Manuscript received by the Editor 5 October 2011; revised manuscript received 16 May 2012; published online 24 August 2012.

¹Petrobras/CENPES/PDGeo/GEOF and Universidade Federal do Rio de Janeiro/COPPE, Rio de Janeiro, Brazil. E-mail: luiz_alberto@petrobras.com.br.

²Universidade Federal do Rio de Janeiro/COPPE, Rio de Janeiro, Brazil. E-mail: webe@coc.ufrj.br.

³The University of Texas at Dallas, Center for Lithospheric Studies, Richardson, Texas, USA. E-mail: mcmec@utdallas.edu.

© 2012 Society of Exploration Geophysicists. All rights reserved.

data experiments show the advantages of incorporating diffraction CFPOs (DCFPOs) into the data to estimate the interval velocity of a deformed layer and to better resolve geometrically complicated structures. In the single channel seismic (SCS) field data profile, DCFPOs carry the only available velocity data; interval velocities of the deep marine sediments at the Blake Ridge are estimated from DCFPOs alone.

ESTIMATING CFPOS FROM DIFFRACTIONS

Seismic data volumes from structurally complex areas are rich in diffractions caused by high curvatures along, and discontinuities in, interfaces. In such environments, traditional CFPO estimation (Berkhout, 1997a, 1997b; Thorbecke, 1997; Bolte, 2003), is difficult to apply. Tracking for events in the differential time shift (DTS) panel does not work if event continuity is broken by diffractions. However, diffractions also can substitute for CFPOs; diffractions can be treated as additional data, rather than as noise.

Consider a source-receiver pair with offset Δx_{SR} in an inhomogeneous medium (Figure 1). The two-way time along the path from the source (S) to the diffractor (A) to the receiver (R) is obtained by adding the line integrals along the curves SA (l_{SA}) and AR (l_{AR}), both with infinitesimal segment lengths dl ;

$$T = \int_{l_{SA}} \frac{dl}{v(x, y, z)} + \int_{l_{AR}} \frac{dl}{v(x, y, z)}. \quad (1)$$

As the S-R offset Δx_{SR} tends to zero, the open angle θ (Figure 1) also tends to zero, and the two integrals in equation 1 become equal; this is the reciprocity principle applied to zero-offset data. For a diffractor, the two-way transit time in a zero-offset section is

$$T = 2 \int_{l_{SA}} \frac{dl}{v(x, y, z)}, \quad (2)$$

and the kinematic part of the Green's function for the diffractor will be half the two-way time T

$$g = \frac{T}{2}. \quad (3)$$

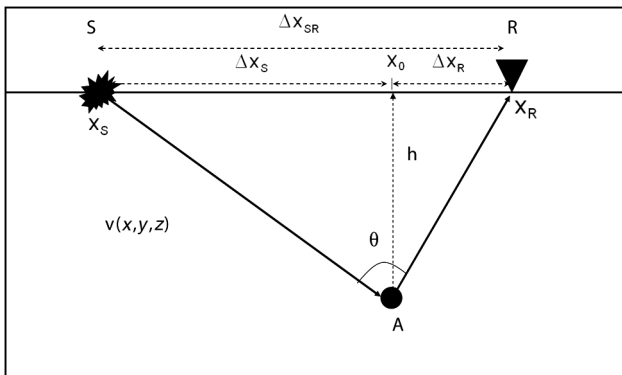


Figure 1. A source (S) and receiver (R) pair sampling a diffractor (A) at depth h inside an inhomogeneous medium.

By extracting diffraction times from common-offset gathers (COGs), CFPOs can be approximated from equation 3, if the minimum offset is much shorter than the diffractor depth.

THE EFFECT OF OFFSET IN THE VELOCITY ESTIMATION

The two-way transit time $t(x)$ for a zero-offset survey for a source-receiver pair located at $(x, 0)$ is

$$t(x) = \sqrt{t_0^2 + \frac{4(x - x_0)^2}{v^2}}, \quad (4)$$

where $t_0 (= 2h/v)$ is the transit time for a receiver (and source) located at x_0 , above the diffractor, h is the depth of the diffractor, and v is the rms velocity at (x, h) .

If a single channel profile for offset Δx_{SR} is incorrectly considered as being a zero-offset survey, what is the error in the estimated velocity? The minimum transit time for this nonzero-offset survey is given by

$$\tau = \sqrt{\frac{4h^2 + \Delta x_{SR}^2}{v^2}}, \quad (5)$$

and it occurs at position

$$x_m = x_0 + \frac{\Delta x_{SR}}{2}. \quad (6)$$

The apparent horizontal velocity along the earth's surface, v_{ap} , from a nonzero-offset COG is not constant, but varies with x_r ; and the nonzero-offset transit time curve is not a hyperbola, even for a homogeneous medium. However, this curve can be approximated by a hyperbolic function and an estimated rms velocity v_{est} can be derived by regression to fit equation 4 by substituting v_{est} for v .

Consider a hypothetical survey where $x_0 = 2500$ m, $h = 1000$ m, velocity $v = 1500$ m/s, and there are 501 receivers spread at every 10 m along a horizontal line on the surface, from 0 to 5000 m. For each horizontal position, v_{est} is estimated by regression of equation 4, but using x_m instead of x_0 , and τ instead of t_0 . The transit time residual r for each offset is calculated by

$$r = \sum_{i=1}^n \frac{1}{n} |t_i - \tau_i|, \quad (7)$$

where n is the number of receivers. The diffractor position x_m in the x -direction is estimated by equation 6 and the diffractor depth is estimated by the minimum two-way transit time τ at each x multiplied by the respective halved v_{est} .

Table 1 shows the residuals, the error in estimated velocity, and the error in diffractor position for offsets from zero to 100 m at intervals of 10 m, assuming the data are all zero-offset traces. The residuals increase with the offset Δx_{SR} , but all are less than 1 ms (less than one sample increment of most seismic surveys). The estimated velocity also increases with offset, but even at the largest (100 m) offset, the error is only 0.027%. The error in depth observed at the largest offset (100 m) is 0.15%. Finally, the error in the position of x_m increases with the offset and is up to 50 m, for the offset of 100 m. Thus, the errors in velocity and depth are negligible for this example. The error in the diffractor position x_m may be corrected by equation 6.

TOMOGRAPHY OVER CFPOS

By using seismic data from a deep source (such as an earthquake), it is possible to estimate the velocity field and the source location (Hegge, 1997). The same principle is used to calculate the CFP positions in depth and the velocity field from CFPOs. Hegge et al. (1996) perform tomography for a five-layer model by placing CFPs equally spaced along the interfaces; for constant velocity layers, iterations converge toward a model very similar to the correct one. Kabir (1997), Hegge et al. (1998), and Kabir and Verschurr (2000) employ layer stripping and incorporate lateral velocity variations in the layers to represent lateral facies changes. Cox (2004) parameterizes the velocity field through Delaunay triangles and inverts converted P-S data.

All of the above studies have uncertainties in discretization of the model. Each estimates the velocity field and the CFP locations, and all use previously estimated CFPOs (Berkhout, 1997a, 1997b; Thorbecke, 1997; Bolte, 2003). CFPO estimation in highly deformed regions is difficult, and gaps in the data space are expected. As a consequence, there will be regions in the model space that are not sampled (or not illuminated) and so will increase ambiguity in the model. Most importantly, conventional CFPOs estimation is not possible for single channel seismic survey data.

Including diffraction CFPOs in the data

The use of diffraction information improves the velocity field and imaging in depth because it adds independent information into the data space. Including diffractions increases the resolution of the seismic velocity (Hegge, 2000; Khaidukov et al., 2004; Moser et al., 2008; Dell and Gajewski, 2011).

After estimation of conventional CFPOs in multichannel seismic data and identifying the main reflections (Berkhout, 1997a, 1997b; Thorbecke, 1997; Bolte, 2003), a search for useful diffractions can begin. To enhance diffractions in a minimum offset COG, specular reflections may be filtered out (Harlan et al., 1984; Fomel et al., 2007; Reshef and Landa, 2009; Dell and Gajewski, 2011). Below, primary reflections are removed using the method that Cao and McMechan (2010) developed for subtraction of multiples.

Comparing the COGs with and without reflections, possible diffraction events are identified. Shape consistency is checked by correlation (equation A-1), and the times of the diffractions that are consistent are divided by two. Then the diffraction CFPOs are cross-correlated with the adjacent conventional CFPOs. Events with abrupt lateral operator changes should be avoided. The use of badly correlated diffraction CFPOs must be validated with local geologic information, or not used.

Diffraction CFPOs are especially useful to estimate the interval velocity field in single channel seismic (SCS) data. In SCS data, there is no way to estimate conventional CFPOs, so the diffraction trajectories with the least radii of curvature are selected (Appendix A). For 2D applications all diffractions used must be in-plane events. After extracting the diffraction CFPOs, the one-way tomographic process starts.

Inversion procedure

Tomographic inversion minimizes a functional Θ (Tarantola, 1987; Aster et al., 2005) represented by the L2 norm of the residuals. The residuals are the difference between the observed

one-way traveltimes of the Green's function \mathbf{g}^{obs} (the conventional and/or diffraction CFPOs transit times) and the calculated ones \mathbf{g}^{calc} , so

$$\Theta = |\mathbf{g}^{\text{obs}} - \mathbf{g}^{\text{calc}}|^2. \quad (8)$$

The inversion process for a model with M parameters is summarized as follows:

- 1) Read and store the N observed time data \mathbf{g}^{obs} ;
- 2) With the model \mathbf{c} , calculate the one-way transit time from the CFPs to the surface (\mathbf{g}^{calc}) by ray tracing;
- 3) Build the sensitivity matrix $\mathbf{A} = \frac{\partial \mathbf{g}}{\partial \mathbf{c}}$ by calculating the derivatives of \mathbf{g} with respect to velocity and CFP positions (Cox, 2004);
- 4) Calculate the updates to the model $\Delta \mathbf{c}$ by

$$\Delta \mathbf{g} - \mathbf{A} \Delta \mathbf{c} = 0, \quad (9)$$

where $\Delta \mathbf{g}$ is the perturbation vector of the time data, and $\Delta \mathbf{c}$ is understood to contain Δv , Δh and Δx ;

- 5) Iterate steps 2 to 4 until the average time residual per record

$$r_{av} = \frac{\Theta}{N} \quad (10)$$

is below a predefined tolerance.

We apply the singular value decomposition (SVD) of the sensitivity matrix at each iteration, through which it is possible to calculate the Moore-Penrose pseudoinverse \mathbf{A}^\dagger (Aster et al., 2005). Then, the update to the model is calculated by

$$\Delta \mathbf{c} = \frac{1}{\Omega} (\mathbf{A} \mathbf{B})^\dagger \Delta \mathbf{g}, \quad (11)$$

where Ω is a factor to control the step size at each iteration and \mathbf{B} is an $M \times M$ diagonal matrix to constrain the sensitivity matrix (Santos et al., 2010). The diagonal elements of \mathbf{B} range from zero to

Table 1. Effect of offset in a constant velocity medium, for estimation of velocity and diffractor coordinates. The correct velocity and diffractor coordinates are 1500 m/s and $(x_m, h) = (2500, 1000)$ m.

Offset (m)	Time residual (s)	Error in velocity (m/s)	Error in depth h (m)	Error in x_m (m)
0	0.00	0.0	0.000	0.000
10	1.58×10^{-5}	0.0	0.025	5.000
20	1.92×10^{-5}	0.0	0.050	10.000
30	2.47×10^{-5}	0.1	0.158	15.000
40	3.79×10^{-5}	0.1	0.233	20.000
50	5.43×10^{-5}	0.1	0.392	25.000
60	7.55×10^{-5}	0.2	0.550	30.000
70	9.38×10^{-5}	0.2	0.758	35.000
80	1.28×10^{-4}	0.3	0.966	40.000
90	1.62×10^{-4}	0.3	1.258	45.000
100	1.85×10^{-4}	0.4	1.516	50.000

one, representing the end-members of constrained and unconstrained parameters, respectively. During the iterative solution, Ω is adapted at each step. If the residual at step $i + 1$ is larger than at the previous step i , a damping factor f is applied to Ω^{-1} . If the residual decreases at step $i + 1$, Ω^{-1} is increased by factor f to accelerate convergence. A suitable value for f is 5%. For non-trivial null data and nontrivial null model spaces, the pseudoinverse provides a solution that corresponds to least squares and minimum length (Aster et al., 2005).

APPLICATION 1: SYNTHETIC DATA SET

The model used for the first two examples represents a region with compressive tectonics. Thin tectonic features leading to thrusts and basal detachment are observed along a 12-km long section. Picking of diffractions is performed in different COGs from 0 to 100 m offset at 10-m intervals. The zero-offset seismic section (Figure 2) shows gently deformed left and right edges and higher deformation in the center.

In both experiments, layer stripping is used because the CFPOs are located along layer boundaries. The velocity field and the layer bottom position is solved for each layer from the top to the bottom of the model. No constraints are applied, so the diagonal terms of matrix \mathbf{B} are all 1. The suitable step size for each iteration is reached with Ω equal 2 in equation 11.

Because of the high-velocity gradients, and the ray-tracing based inversion kernel, a 31×31 sample smoothing is applied to the model in both experiments. A secondary benefit of the smoothing is that

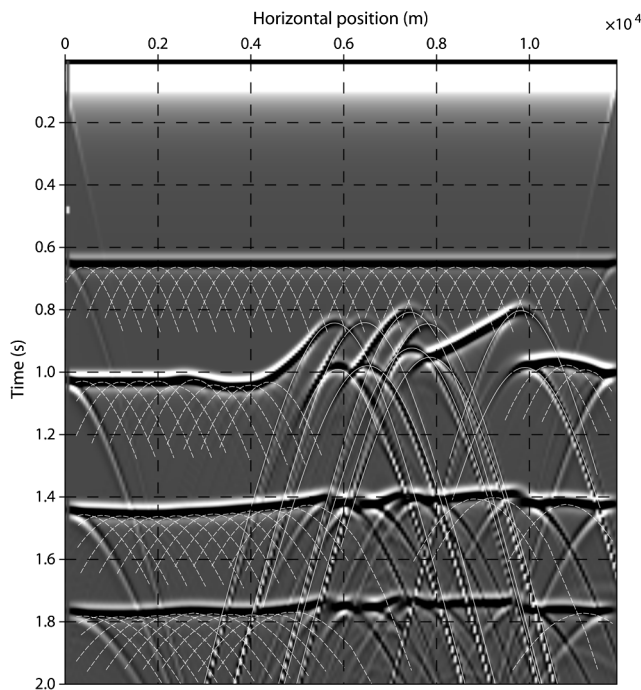


Figure 2. Overlay of the zero-offset section with conventional CFPOs (the white dashed lines) and diffraction CFPOs (the white continuous line). The seismogram is plotted in one-way time to fit with the CFPOs. The modeling edge artifacts (the four hyperbolic curves whose apexes are at 0.65 s, 1.05 s, 1.45 s, and 1.80 s) on the left and right edges are not considered in the analysis.

Snell's law does not have to be explicitly applied at the interfaces (Hegge, 2000).

For experiment 1, the data space contains the CFPO transit times (the dashed white lines in Figure 2); in experiment 2, DCFPO transit times (the continuous white lines in Figure 2) are added. The model space of both experiments consists of constant velocity layers and the CFP (x, z) coordinates. The a priori model contains CFPs positioned horizontally along the layer bottoms at constant depths of 1000 m, 1600 m, 2450 m, and 3300 m. The a priori velocities for the first (the top) to the fourth (the bottom) layers are 1500, 1500, 1800, and 2400 m/s.

The largest acceptable traveltime average residual per observation (the convergence condition) for each layer is set to 0.6 ms; the residuals are calculated from the corresponding observed and calculated CFPOs (equation 10). For the first layer, only one iteration is required as the estimated a priori model is the same as the correct one. In experiment 1, no more than four iterations are necessary to achieve convergence to 0.6 ms for velocity and CFP position for each layer (Figure 3a). Figure 4a shows an overlay of the target velocity model and the inverted interfaces. The estimated velocities and structures are plotted together in Figure 4b. The average velocity error per point, calculated by

$$e = \frac{1}{M} |\mathbf{v}^{\text{obs}} - \mathbf{v}^{\text{calc}}|, \quad (12)$$

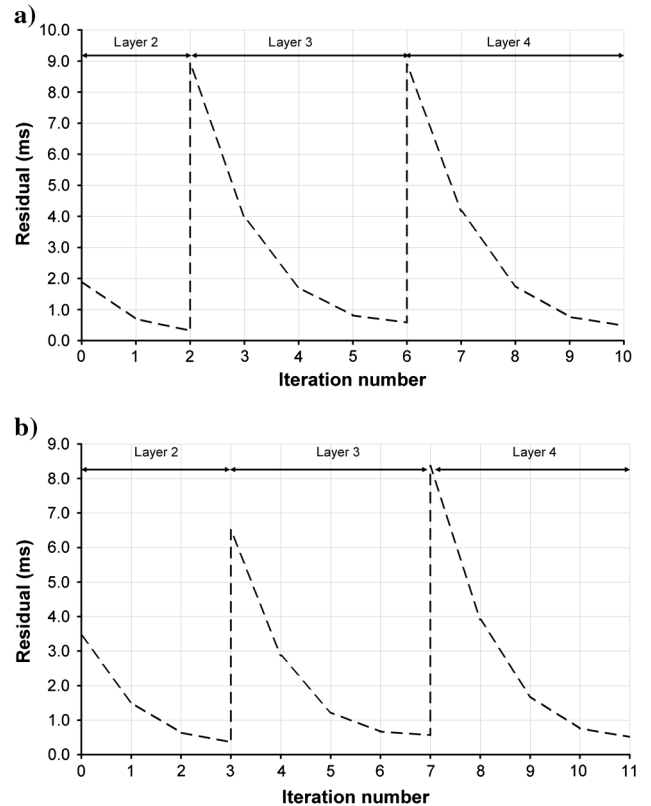


Figure 3. (a) Residuals at each iteration of experiment 1 for the synthetic data set. (b) Residuals at each iteration of experiment 2 for the synthetic data set. In (a) and (b), the residual curves for layers 2, 3, and 4 are plotted together, so the iteration numbers are listed cumulatively.

is 0.038 m/s. The number of velocity points in the model is M , \mathbf{v}^{obs} is the target model, and \mathbf{v}^{calc} is the estimated velocity model.

In experiment 2, the inversion process, the parameterization, and the residual tolerance are the same as for experiment 1, but the information carried by diffractions (the white solid lines in Figure 2) also are used, to give a more complete data space. An important step is to merge the conventional CFPs and diffractions and then to sort them in order from left to right. For this, the starting diffractor positions on the x -axis are estimated from the corresponding operator apex x -coordinates. These added data allow a better estimation and interpolation of the faulted horizon.

The convergence behavior of experiment 2 is in Figure 3b. The use of DCFPOs increases the structural resolution (Figure 4c) and delivers a final model closer to the actual one (Figure 4d). The relative error calculated for experiment 2 by equation 12 is 0.035 m/s per point.

For both synthetic data experiments, no more than four iterations were required for convergence of each layer. The error of the velocity field for experiment 1 is higher than for experiment 2 because of a gap of information occurs in 1 exactly where there are abrupt changes in the model (Figures 2 and 4a).

In experiment 1, the structures estimated by inversion at the bottom of layer 2 are too smooth (Figure 4a). Experiment 2 locates the CFPs close to their correct positions (Figure 4c), and thus delivers a better structural image. This is the result of the conventional and diffraction CFPs being combined together as independent constraints when they belong to the same reflector. In both experiments, an underestimation of layer velocities is observed in deeper layers; layer-stripping accumulates errors from the shallower layers to the deeper ones.

Because of picking inaccuracies and the low-dominant frequency of the recorded wavelet (25 Hz), all COGs with offsets between 0 and 60 m delivered very similar diffraction curves. Equation 6 is employed to minimize the errors in horizontal coordinates of the diffractor for offsets larger than 60 m.

APPLICATION 2: SINGLE-CHANNEL SEISMIC DATA SET

The field data example of DCFPO-based tomography uses a 60 km segment of the single-channel seismic line 09 surveyed over the Blake Ridge by the USGS (Taylor et al., 1999) in a southwest–northeast orientation (Figure 5). This line was chosen for the current study because it is richer in point diffractions than the other available lines in that area.

The survey was acquired with a constant offset of 10 m, and a time-sampling increment of 2 ms (Taylor et al., 1999). The line was binned to 4136 equally spaced traces. With the offset of only 10 m, on the basis of the results in Table 1, we treat the data as zero offset.

The processing flow for the data includes predictive filtering (to yield a wavelet by trace autocorrelation for each trace), band-pass (8–110 Hz) filtering, and a geometrical spreading correction. For enhancement of nonspecular events, the shallow coherent reflections were subtracted from the processed section using the technique of Cao and McMechan (2010) applied to the primary specular reflections. Comparing the processed section with and without reflections, all probable point diffractions were identified; some events were omitted because of their locally large radii of curvature. The horizontal aperture of the DCFPOs at the surface ranges from 1800 to 2300 m, with angle apertures large enough that most DCFPO operators overlap with their neighbors and thus reduce velocity-depth ambiguities (Figure 6).

The velocity model is discretized by 2D cubic splines and global inversion is applied instead of the layer stripping approach, because the diffractors do not define layer boundaries as in the synthetic examples above. The spline mesh is rectangular with variable vertical node spacing finer than the horizontal. The vertical node

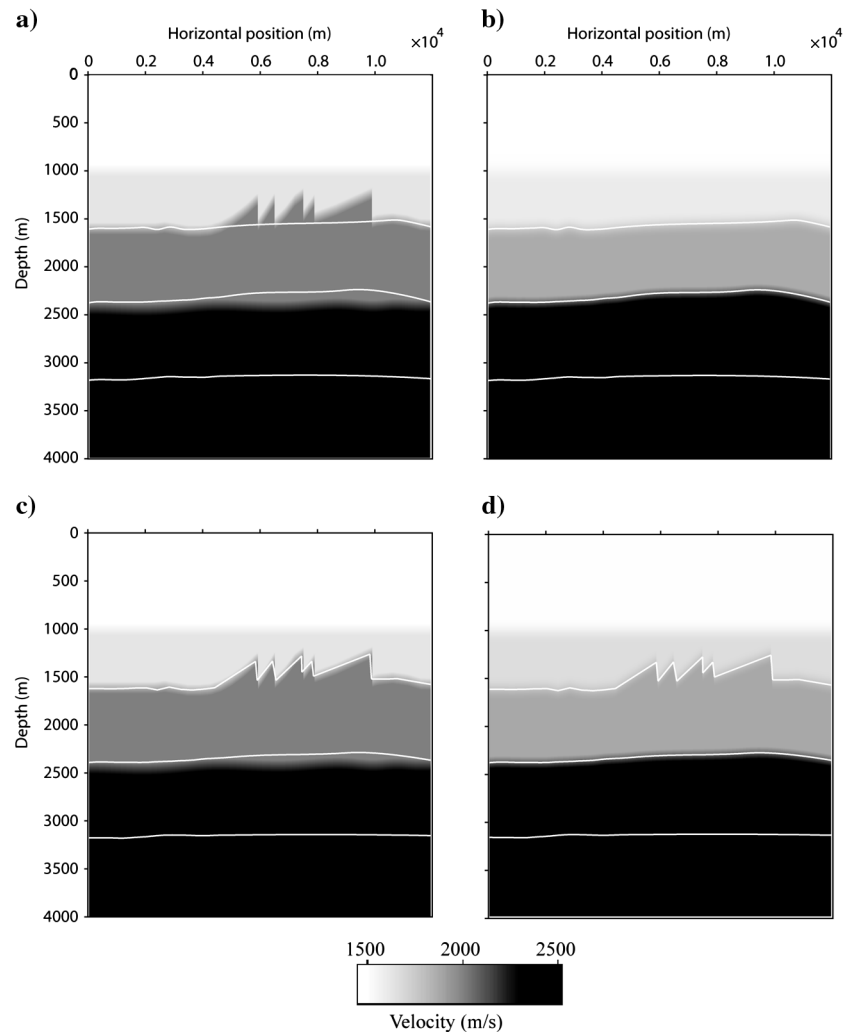


Figure 4. (a) Overlay of the real model and the calculated CFPs of experiment 1. (b) Velocity model estimated by the inversion of conventional CFPs. (c) Overlay of the real model and the calculated CFPs of experiment 2, showing better structural resolution than in experiment 1. (d) Velocity model calculated through the inversion of conventional and diffractions CFPs together. All figures have the same grayscale.

spacing used is: 538.0 m from 0.0 to 2690.0 m depth, 53.8 m from 2690 m to 3129.4 m depth, and 107.6 m from 3120.4 m to 3600 m depth. The horizontal distance between nodes decreases from 10760.0 m at the left side to 5380.0 m at the right. The mesh is

adjusted for the model dimensions, is suitable for the observed bathymetric characteristics, and adjusts to the data availability; thus, inversion artifacts are reduced compared to what they would be for regular meshes.

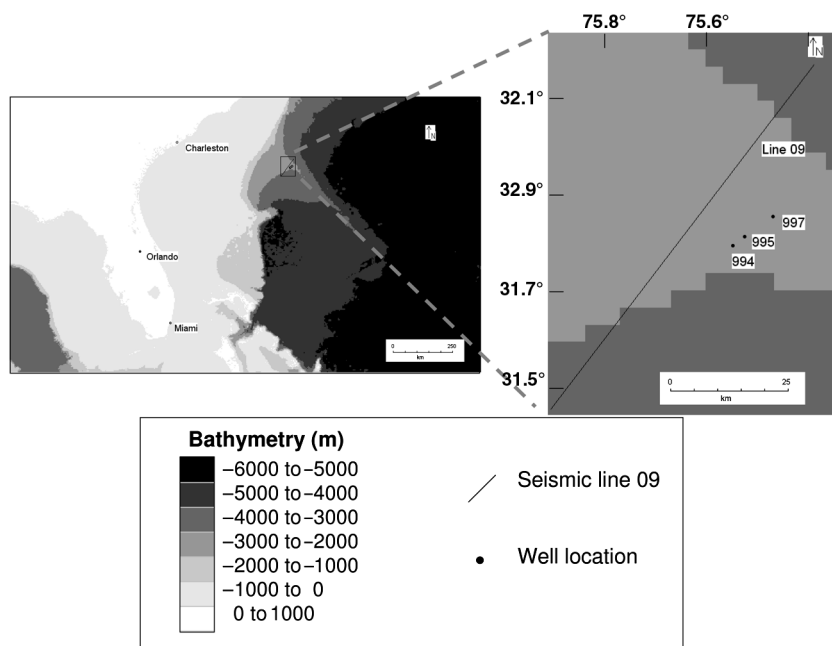


Figure 5. Well locations and seismic line 09 on the Blake Ridge.

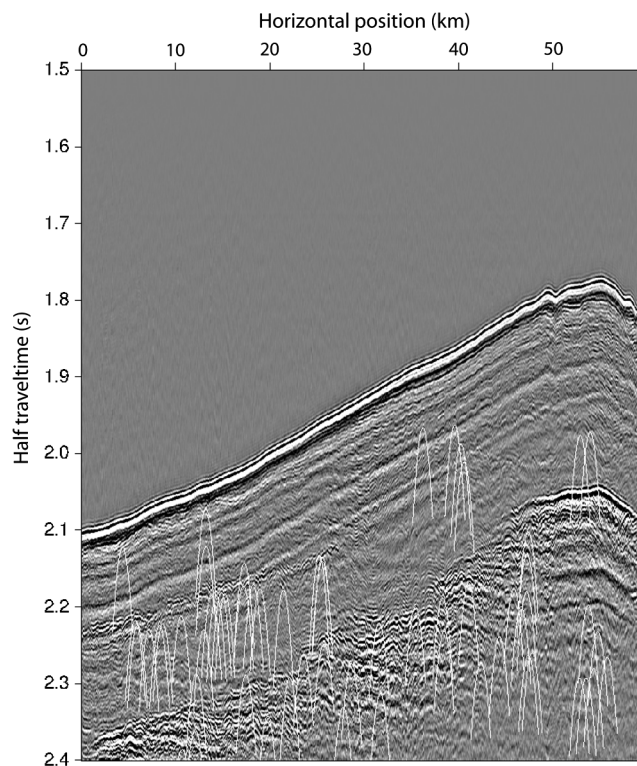


Figure 6. USGS seismic line 09 with halved time and diffraction CFP operators (white lines).

In the a priori model, the known velocity of water of 1500 m/s (Klitgord et al., 1994) is used above the sea bottom. A vertical fifth-order polynomial function

$$v(x, \Delta z) = \sum_{i=0}^5 C_i (\Delta z)^i, \quad (13)$$

referenced to the sea floor $v(x, \Delta z)$, varying from 1550 to 1750 m/s (Carmichael, 1982), represents the sediment pile and simulates the combined effects of compaction and the hydrated zone. The coefficients C_i are calculated by regression of the average velocities from wells 994, 995, and 997 (Paull et al., 2000; Lu and McMechan, 2002), which are 9 to 11 km away from line 09. Coefficients C_0 to C_5 are 1516.19, 1.64838e-01, $-1.24340e-02$, 2.15813e-03, $-5.59170e-05$, and 3.92534e-07, respectively; Δz is the depth in meters below the sea-floor (mbsf).

During the inversion only the water column is constrained by setting the corresponding elements of the sensitivity matrix \mathbf{B} in equation 11 to zero. All other elements on the diagonal of the matrix \mathbf{B} are set to one. The step size is adjusted

with $\Omega^{-1} = 0.2$. After 28 iterations, the inversion converged to the velocity field in Figure 7b with an average time residual (equation 10) below 0.3 ms (Figure 8). The time residuals for the a priori model already are small, so the CFPO inversion fine-tunes the starting velocity field.

Compare our estimated velocity field with the features observed in the seismic section and with the layer-based multichannel two-way time tomographic results of Tinivella and Lodolo (2000); the latter is applied to two profiles located east of line 09. The seismic section in Figure 6 is time-to-depth converted and three reflectors are interpreted inside the sediment pile; HZA, HZB, and the BSR (the bottom simulating reflector) (Figure 7a and 7b). HZA and BSR correspond to horizons 2 and 3 of Tinivella and Lodolo (2000).

Along the flank of the structure, the velocity field follows the shape of the reflectors between the sea floor and horizon HZA, but there are lateral velocity gradients (at I in Figure 7b). Beneath the apex of the sea floor topography, HZA crosses velocities lower than the background (at II in Figure 7b) that correlate to a visible disturbance of the reflections (Figure 7a) and with some offset of the sea floor (see the small mound at the apex of the seafloor topography). The estimated velocities between the sea bottom and HZA are lower than those found in Tinivella and Lodolo (2000).

Below horizon HZB, the velocity ranges from 1650 to 1750 m/s (Figure 7b). Guerrin et al. (1999) interpret this as being caused by methane hydrate acting as intergranular cement and increasing the bulk modulus of the host sediment. Below HZB, between horizontal positions of 0 and 20 km there is a zone with higher velocities (III in Figure 7b); this zone appears in the time-to-depth converted seismic section (Figure 7a) as a fairly homogeneous seismofacies delimited

by concordant levels with disturbed nonspecular reflections at its top and bottom. A high-velocity zone (at IV in Figure 7b) is observed beneath to the apex of the sea floor at depths between HZB and BSR. The proximity to the apex promotes a higher methane availability, and thus favors a higher concentration of hydrates in the gas hydrate stability zone (GHSZ) and increases the velocity.

It was not possible to identify the low velocity associated with the BSR apex, indicated by the high negative amplitude (at V in Figure 7a and 7b), and associated with a free-gas interval in well 997. Tinivella and Lodolo (2000), using a layer-based discretization, underestimate the free-gas layer thickness by a factor of three compared to that estimated from VSP data. The available DCFPO

and the spline discretization do not have sufficient resolution to identify this interval. According to Guerrin et al. (1999) the BSR marks the top of the occurrence of free gas, not the bottom of GHSZ so, below the BSR, free gas may coexist with methane hydrates. Thus, the estimated velocity is an average of the high-velocity hydrate-bearing and the low-velocity gas-bearing sediments.

The inversion performed by Tinivella and Lodolo (2000) is limited to their deepest mappable horizon four, just below the BSR. By using available diffractions we investigate a deeper region. In this sense, DCFPO tomography and multichannel reflection tomography are complementary.

CONCLUSIONS

We propose a method to estimate the velocity field using the kinematic information carried by diffractions. It is based on the principles of CFP tomographic inversion. For complicated structures, and with multichannel seismic data, diffractions may be added to conventional CFPOs to increase the resolution of the structure and velocity fields. For single channel seismic data, DCFPO tomography delivers the velocity field with low computational effort wherever real diffractions are observed. Equation 11 does indeed work for the inversion with the SVD solver. By using the DCFPOs, we estimate a velocity field that is geologically coherent and agrees with the velocity trends estimated by multichannel seismic data.

ACKNOWLEDGMENTS

We thank Petrobras for the financial support and the physical facilities for this research. We would like to thank the geophysics team at Petrobras Research Center and Petrobras headquarters in Rio de Janeiro for very helpful discussions and suggestions. We also would like to thank André Bulcão for the synthetic data used in this work. This paper is Contribution no. 1234 from the Geoscience Department at the University of Texas at Dallas.

APPENDIX A

WHICH EVENTS SHOULD BE USED IN DIFFRACTION CFPO TOMOGRAPHY?

Diffraction CFPO tomography will fail if a mapped event in a minimum offset COG is not a real diffraction from a point. Diffractions should be enhanced before picking because their energy is usually weaker than the reflections (Berkovitch et al., 2009). Specular reflections present in a COG may be filtered (Harlan et al., 1984; Fomel, 2002; Fomel et al., 2007; Reshef and Landa, 2009; Dell and Gajewski, 2011). These methods may produce events that resemble diffractions, but are not generated by point diffractors. Separation of reflections and diffractions can never be exact (Fomel et al., 2007). Curved surfaces or even small plane segments can deliver diffraction-like features (hyperboloids) in seismic sections. However, their shapes are incompatible with those of

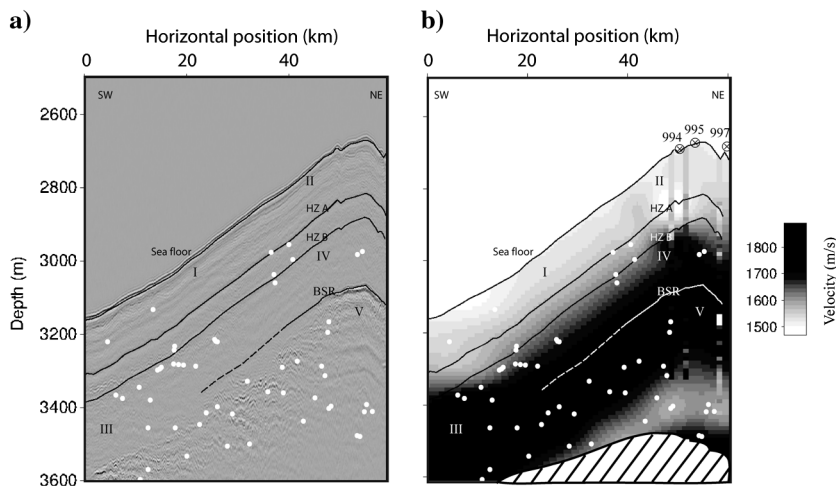


Figure 7. (a) Seismic section (line 09) time-to-depth converted with the calculated velocity. Beneath the sea floor there are three interpreted horizons (the black lines) HZA, HZB, and BSR (the bottom simulating reflector above the gas zone). The white-filled circles are the diffractor positions determined during the inversion of the DCFPOs. (b) Composite section containing the inversion result over DCFPOs of line 09 and projections of velocity logs from wells 994, 995, and 997 from left (southwest) to right (northeast). The legend of the velocity field is valid only for (b). The lined zone at the bottom of (b) has no data. See the text for additional details about the features labeled I, II, III, IV, and V.

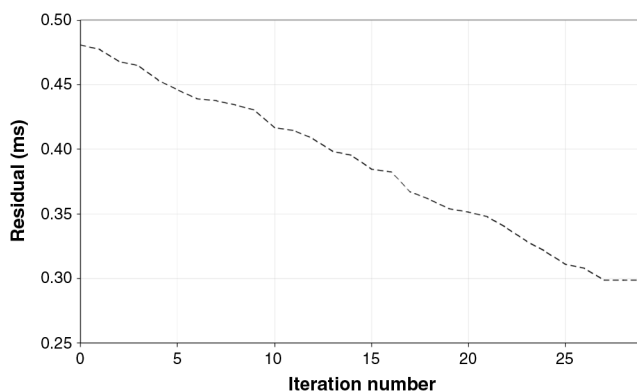


Figure 8. Residuals for the tomographic inversion of the Blake Ridge SCS data.

Table A-1. Experiments of sinusoidal interface exploding reflectors for different α , for identical sources with dominant wavelength of 100 m. The diffractor behavior of the peaks and troughs is observed only for models with $\alpha < 16$.

Model	α	Source wavelength (m)	Diffractor behavior
1	10	100	Yes
2	12	100	Yes
3	14	100	Yes
4	16	100	No
5	18	100	No
6	20	100	No

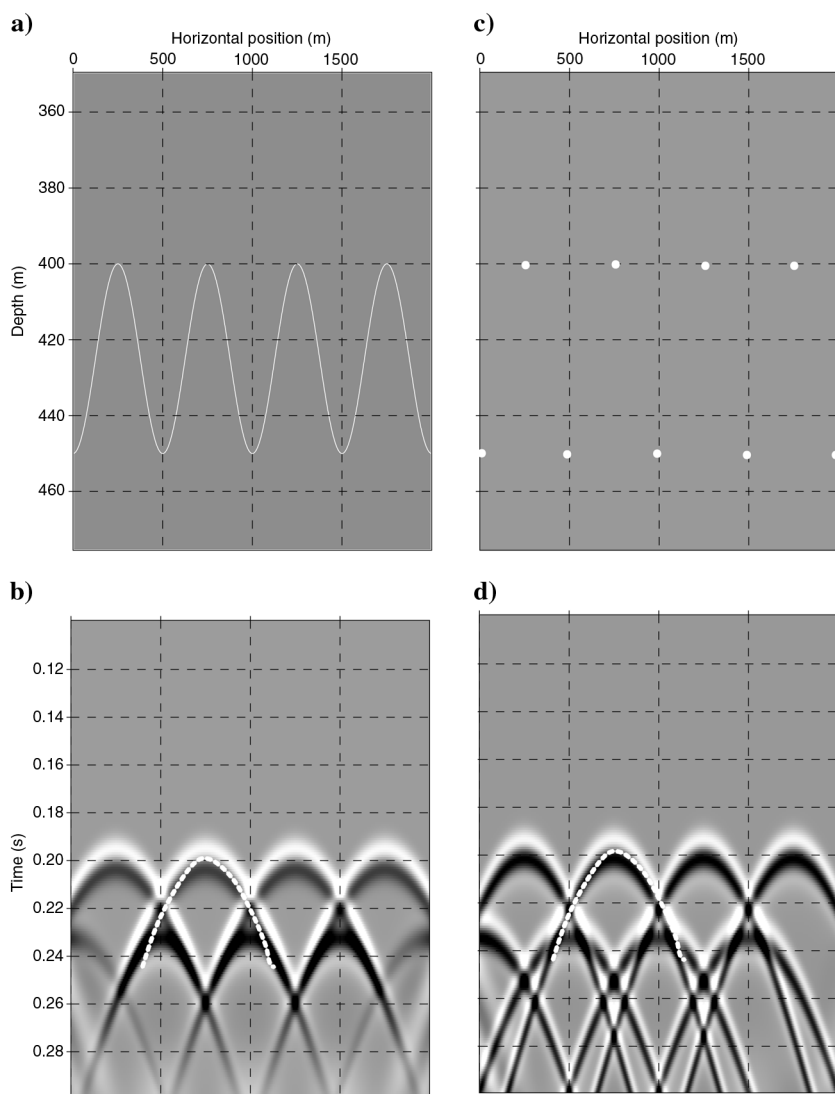


Figure A-1. (a) Model for the sine curve exploding reflector with amplitude of 25 m and wavelength of 500 m in a constant velocity media of 2000 m/s. (b) Seismogram corresponding to the model in (a). The white dashed line maps a real diffraction at the corresponding peak. Peaks and troughs of the sine curve do not behave as diffractors. (c) Model for a series of diffractors, represented by white-filled circles, located at peaks and troughs of the same sine curve in (a). (d) Seismogram corresponding to the model in (c). The white dashed line maps a real diffraction.

diffractions caused by the actual velocity field, and so should not be used for tomographic velocity analysis. Additionally, a linear geologic feature such as a channel or a syncline/anticline, can produce a cylinder-like wavefront rather than a point diffraction which, if sampled obliquely to its dip direction, will have many of the properties of a diffraction, but its shape also will be incompatible with the velocity.

Consider now, a hypothetical 2D survey line that is parallel to the geologic dip direction. When the radius of curvature of a folded interface is much less than its wavelength, or the interface is terminated by a fault, pinchout, or unconformity, such segments behave as diffractors (Sheriff and Geldart, 1999).

Let there be a sinusoidal reflector with wavelength (λ_0) of amplitude (A_0) ratio of α (Figure A-1a). An exploding reflector seismic modeling experiment was performed for this structure with $\lambda_0 = 500$ m, $A_0 = 25$ m, or $\alpha = 20$, (Figure A-1a), using a 20 Hz Ricker wavelet, and with a background velocity model of 2000 m/s. Receivers were spread equally spaced (at 1 m) along the surface; the resulting seismogram is in Figure A-1b. In a second simulation, point diffractors located only at the peak and trough positions are used as sources (Figure A-1c); the resulting seismogram (Figure A-1d) exhibits real diffractions.

Diffractions (the white dashed curves in Figure A-1b and A-1d) do not fit the hyperbola-like signals for the sine peaks of Figure A-1b; the resulting curve is the summation of point diffraction responses over the apex and flanks of the sinusoidal structure. Because of the summation, the curve shapes are broader than those of point diffractions curves (the white dashed curve in Figure A-1b), and are not consistent with the actual velocity of 2000 m/s, but with a higher one.

A series of similar experiments were performed for α varying between 10 and 20 for a dominant source wavelength of 100 m (Table A-1). For sine-like structures, the diffraction behavior is not observed for α greater than or equal to 16. Diffraction behaviors occur when the radii of curvature are smaller than $\frac{1}{16}$ of the source dominant wavelength. Thus we expect that various structures, such as pinchouts, faults, kink-folds, and channels (incised valleys) can generate diffraction-like signals that are useful for diffraction CFPO tomography.

If there is no a priori information about the subsurface, no way to reduce doubt about the diffraction character of a curve in a seismic section is to check its persistence in shape and position of its apex across shot gathers. The kinematic part of a real diffraction will exhibit the same shape in different shot and receiver gathers.

Landa et al. (1987) detect diffractions by correlations of seismic data in common mid-point, common offset, and common shot gathers. If we crosscorrelate the kinematic response of

diffraction A in shot gather one with its response in shot gather two we find

$$C_{SG}(x_{s1,s2}, x_r, t) = g_{SG}(x_{s1}, x_r, t) \otimes_t g_{SG}(x_{s2}, x_r, t) \\ = \delta(t - [t_{s1,A} - t_{s2,A}]), \quad (\text{A-1})$$

where the symbol \otimes_t means trace-by-trace crosscorrelation in the time domain. The panel $C_{SG}(x_{s1,s2}, x_r, t)$ shows a horizontal line at time $t_{s1,A} - t_{s2,A}$ for real diffractions. The result is the transit time difference between sources 1 and 2 to diffractor A (equation A-1).

Finally, picked diffractions may be compared with neighboring CFPOs obtained conventionally in the same common-offset-gather. The shape of a diffraction CFPO and a neighboring conventional CFPO are similar. Abrupt changes in adjacent operators represent a high lateral gradient of the velocity field. If a priori knowledge does not support high gradients, anomalous operators must be avoided because they probably are out-of-plane propagation.

REFERENCES

- Al-Yahya, K., 1989, Velocity analysis by iterative profile migration: *Geophysics*, **54**, 718–729, doi: [10.1190/1.1442699](https://doi.org/10.1190/1.1442699).
- Aster, R. C., B. Borchers, and C. H. Thurber, 2005, *Parameter estimation and inverse problems*: 1st ed., Elsevier Academic Press.
- Berkhout, A. J., 1997a, Pushing the limits of seismic imaging, Part I: Prestack migration in terms of double dynamic focusing: *Geophysics*, **62**, 937–954, doi: [10.1190/1.1444201](https://doi.org/10.1190/1.1444201).
- Berkhout, A. J., 1997b, Pushing the limits of seismic imaging, Part II: Integration of prestack migration, velocity estimation, and AVO analysis: *Geophysics*, **62**, 954–969, doi: [10.1190/1.1444202](https://doi.org/10.1190/1.1444202).
- Berkhout, A. J., and C. P. A. Wapenaar, 1989, One-way versions of the Kirchhoff integral: *Geophysics*, **54**, 460–467, doi: [10.1190/1.1442672](https://doi.org/10.1190/1.1442672).
- Berkovitch, A., I. Belfer, Y. Hassin, and E. Landa, 2009, Diffraction imaging by multifocusing: *Geophysics*, **74**, no. 6, WCA75–WCA81, doi: [10.1190/1.3198210](https://doi.org/10.1190/1.3198210).
- Billette, F., and G. Lambaré, 1998, Velocity macro-model estimation from seismic reflection data by stereotomography: *Geophysical Journal International*, **135**, 671–690, doi: [10.1046/j.1365-246X.1998.00632.x](https://doi.org/10.1046/j.1365-246X.1998.00632.x).
- Bishop, T. N., K. P. Bube, R. T. Cutler, R. T. Langan, P. L. Love, J. R. Resnick, R. T. Shuey, D. A. Spindler, and H. W. Wyld, 1985, Tomographic determination of velocity and depth in laterally varying media: *Geophysics*, **50**, 903–923, doi: [10.1190/1.1441970](https://doi.org/10.1190/1.1441970).
- Bolte, J. F. B., 2003, Estimation of focusing operators using the common focal point method: Ph.D. thesis, Delft University of Technology.
- Burnett, W., S. Fomel, and R. Bansal, 2011, Diffraction velocity analysis by path-integral seismic imaging: 81st Annual International Meeting, SEG, Expanded Abstracts, 3898–3902.
- Cao, J., and G. A. McMechan, 2010, Multiple prediction and subtraction from apparent slowness relations in 2D synthetic and field ocean-bottom cable data: *Geophysics*, **75**, no. 6, V89–V99, doi: [10.1190/1.3506145](https://doi.org/10.1190/1.3506145).
- Carmichael, R. S., 1982, *Handbook of physical properties of rocks*, 2: CRC Press.
- Cox, B. E., 2004, Tomographic inversion of focusing operators: Ph.D. thesis, Delft University of Technology.
- Dell, S., and D. Gajewski, 2011, Common-reflection-surface-based workflow for diffraction imaging: *Geophysics*, **76**, no. 5, S187–S195, doi: [10.1190/geo2010-0229.1](https://doi.org/10.1190/geo2010-0229.1).
- Dix, C. H., 1955, Seismic velocities from surface measurements: *Geophysics*, **20**, 68–86, doi: [10.1190/1.1438126](https://doi.org/10.1190/1.1438126).
- Fomel, S., 2002, Applications of plane-wave destruction filters: *Geophysics*, **67**, 1946–1960, doi: [10.1190/1.1527095](https://doi.org/10.1190/1.1527095).
- Fomel, S., 2003, Time-migration velocity analysis by velocity continuation: *Geophysics*, **68**, 1662–1672, doi: [10.1190/1.1620640](https://doi.org/10.1190/1.1620640).
- Fomel, S., E. Landa, and M. T. Taner, 2007, Poststack velocity analysis by separation and imaging of seismic diffractions: *Geophysics*, **72**, no. 6, U89–U94, doi: [10.1190/1.2781533](https://doi.org/10.1190/1.2781533).
- Guerrin, G., D. Goldberg, and A. Meltser, 1999, Characterization of in situ elastic properties of gas hydrate-bearing sediments on the Blake Ridge: *Journal of Geophysical Research*, **104**, 17781–17795, doi: [10.1029/1999JB900127](https://doi.org/10.1029/1999JB900127).
- Harlan, W. S., J. F. Claerbout, and F. Rocca, 1984, Signal/noise separation and velocity estimation: *Geophysics*, **49**, 1869–1880, doi: [10.1190/1.1441600](https://doi.org/10.1190/1.1441600).
- Hegge, R. F., 1997, Velocity model estimation by inversion of focusing operators: 67th Annual International Meeting, SEG, Expanded Abstracts, 1456–1459.
- Hegge, R. F., 2000, Seismic macromodel estimation by inversion of focusing operators: Ph.D. thesis, Delft University of Technology.
- Hegge, R. F., J. F. B. Bolte, D. J. Verschuur, J. T. Fokkema, and A. J. W. Duijndam, 1999, CFP operator estimation and inversion demonstrated on a field data set — Part II: velocity estimation: 69th Annual International Meeting, SEG, Expanded Abstracts, 1500–1503.
- Hegge, R. F., and J. T. Fokkema, 1996, Macro model updating by global inversion of CFP operators: 66th Annual International Meeting, SEG, Expanded Abstracts, 707–710.
- Hegge, R. F., J. T. Fokkema, and A. J. W. Duijndam, 1998, Using focusing operators to estimate velocity models: 68th Annual International Meeting, SEG, Expanded Abstracts, 1608–1611.
- Kabir, M. M. N., 1997, Velocity Estimation of the complex subsurface using the common focus point technology: Ph.D. thesis, Delft University of Technology.
- Kabir, M. M. N., and D. J. Verschuur, 2000, A constrained parametric inversion for velocity analysis based on CFP technology: *Geophysics*, **65**, 1210–1222, doi: [10.1190/1.1444813](https://doi.org/10.1190/1.1444813).
- Khaidukov, V., E. Landa, and T. J. Moser, 2004, Diffraction imaging by focusing-defocusing: An outlook on seismic superresolution: *Geophysics*, **69**, 1478–1490, doi: [10.1190/1.1836821](https://doi.org/10.1190/1.1836821).
- Klitgord, K. D., and C. M. Schneider, 1994, Geophysical database of the East Coast of the United States Northern Atlantic Margin: velocity analysis: U.S. Geological Survey Open-File Report, 94–192.
- Landa, E., V. Shtivelman, and B. Gelchinsky, 1987, A method for detection of diffracted waves on common-offset sections: *Geophysical Prospecting*, **35**, 359–373, doi: [10.1111/j.1365-2478.1987.tb00823.x](https://doi.org/10.1111/j.1365-2478.1987.tb00823.x).
- Liu, J., Y. Luo, and Y. Yao, 2006, Tomographic inversion based on CFP technology: 76th Annual International Meeting, SEG, Expanded Abstracts, 3388–3392.
- Lu, S., and G. A. McMechan, 2002, Estimation of gas hydrate and free gas saturation, concentration and distribution from seismic data: *Geophysics*, **67**, 582–593, doi: [10.1190/1.1468619](https://doi.org/10.1190/1.1468619).
- McKay, S., and R. Abma, 1992, Imaging and velocity estimation with depth-focusing analysis: *Geophysics*, **57**, 1608–1622, doi: [10.1190/1.1443228](https://doi.org/10.1190/1.1443228).
- Moser, T. J., and C. B. Howard, 2008, Diffraction imaging in depth: *Geophysical Prospecting*, **56**, 627–641, doi: [10.1111/j.1365-2478.2007.00718.x](https://doi.org/10.1111/j.1365-2478.2007.00718.x).
- Paull, C. K., R. Matsumoto, P. J. Wallace, and W. P. Dillon, 2000, Proceedings of the Ocean Drilling Program, Scientific Results, **164**, 1–318.
- Reshet, M., and E. Landa, 2009, Post-stack velocity analysis in the dip-angle domain using diffractions: *Geophysical Prospecting*, **57**, 811–821, doi: [10.1111/j.1365-2478.2008.00773.x](https://doi.org/10.1111/j.1365-2478.2008.00773.x).
- Rijzen, M. J., D. J. Verschuur, and A. Gisolf, 2004, 3D focusing operator estimation using sparse data: 74th Annual International Meeting, SEG, Expanded Abstracts, 2048–2051.
- Santos, L. A., D. M. Soares Filho, A. Bulcão, C. E. Theodoro, W. J. Mansur, and G. A. McMechan, 2010, Tomographic inversion over diffraction CFP operators in structurally complex areas: 80th Annual International Meeting, SEG, Expanded Abstracts, 4275–4279.
- Sava, P., B. Biondi, and J. Etgen, 2005, Wave-equation migration velocity analysis by focusing diffractions and reflections: *Geophysics*, **70**, no. 3, U19–U27, doi: [10.1190/1.1925749](https://doi.org/10.1190/1.1925749).
- Sheriff, R. E., and L. P. Geldart, 1999, *Exploration seismology*: Cambridge University Press.
- Tarantola, A., 1987, Inverse problem theory: Methods for data fitting and model parameter estimation: Elsevier.
- Taylor, M. H., W. P. Dillon, C. H. Anton, and W. Danforth, 1999, Seismic-reflection surveys of the Blake Ridge, R/V CAPE HATTERAS 1992 and 1995: Data acquisition, navigation and processing: U.S. Geological Survey Open-File Report, 99–372, <http://pubs.usgs.gov/of/1999/of99-372/>.
- Thorbecke, J. W., 1997, Common focus point technology: Ph.D. thesis, Delft University of Technology.
- Tinivella, U., and E. Lodolo, 2000, The Blake Ridge bottom-simulating reflector transect: tomographic velocity field and theoretical model to estimate methane hydrate quantities: Proceedings of the Ocean Drilling Program, Scientific Results, **164**, 273–318.
- Woodward, M. J., D. Nichols, O. Zdraveva, P. Whitfield, and T. Johns, 2008, A decade of tomography: *Geophysics*, **73**, no. 5, VE5–VE11, doi: [10.1190/1.2969907](https://doi.org/10.1190/1.2969907).